Laser & Photonics Reviews

LASER & PHOTONICS REVIEWS

www.lpr-journal.org

RESEARCH ARTICLE

Enhancing the Quality Factors of Guided Resonances via Rational Symmetry Breaking

Shiwang Yu[1] | Yuexin Sun[1] | Duk-Yong Choi[2] | Zhancheng Li[1] | Wenwei Liu[1] | Wenyuan Zhou[1] | Hua Cheng[1] | Shuqi Chen[1,3,4]

[1]The Key Laboratory of Weak Light Nonlinear Photonics, Ministry of Education, School of Physics and TEDA Institute of Applied Physics, Nankai University, Tianjin300071, China | [2]Laser Physics Centre, Research School of Physics, Australian National University, Canberra, ACT 2601, Australia | [3]School of Materials Science and Engineering, Nankai University, Tianjin300350, China | [4]The Collaborative Innovation Center of Extreme Optics, Shanxi University, Taiyuan, Shanxi 030006, China

Correspondence: Zhancheng Li (zcli@nankai.edu.cn) | Hua Cheng (hcheng@nankai.edu.cn) | Shuqi Chen (schen@nankai.edu.cn)

Received: 10 July 2025 | **Revised:** 6 October 2025 | **Accepted:** 21 October 2025

Keywords: bound states in the continuum | Brillouin zone folding | guided mode resonances | high quality factors | symmetry-breaking metasurfaces

ABSTRACT

Optical resonators supporting quasi-bound states in the continuum (quasi-BICs) and quasi-guided modes (quasi-GMs) induced by structural symmetry-breaking perturbations can confine light with exceptionally high quality (Q) factors. However, their Q factors are highly sensitive to the wavevector and structural asymmetry parameters. Merging multiple BICs and Brillouin zone folding can substantially enhance the Q factor robustness of quasi-BICs and quasi-GMs against symmetry-breaking perturbations, but is limited by the specific mode types and modest asymmetry levels. Here, we demonstrate that the Q factors of these modes can be simultaneously enhanced even under significant levels of asymmetry. By rationally engineering the symmetry breaking, we achieve an order-of-magnitude improvement in the Q factors compared to previously reported Brillouin-zone-folding-induced guided resonances. Group symmetry analysis and coupling amplitude calculations reveal that the enhancement of the Q factor originates from the suppression of radiative losses by selectively breaking certain symmetries while preserving others. We further experimentally validated that the Q factors of quasi-GMs exhibit substantial enhancement, surpassing those of conventional designs. Our strategy provides an effective approach for realizing high-Q resonances under significant symmetry-breaking conditions, thus relaxing the stringent requirements on nanofabrication tolerance.

1 | Introduction

Optical resonators that enable strong light confinement are essential for advancing a wide range of important applications, such as low-threshold nanolasers [1–5], nonlinear signal enhancement [6–8], optical modulators [9, 10], and enhanced exciton-photon coupling [11–13]. The ability of a resonator to confine light is characterized by the quality (Q) factor, defined as $Q = \omega/2\gamma$, where ω and γ are the resonant frequency and leakage rate of the optical resonance, respectively [14, 15]. Recently, bound states in the continuum (BICs) and quasi-guided modes (quasi-GMs) have been proposed to achieve ultrahigh-Q resonances in periodically extended nanostructures [14, 16–21]. GMs correspond to bound states below the light line, while BICs represent discrete localized states above the light line, neither of which can couple with the far field. In practice, BICs can transform into quasi-BICs by altering wavevectors or nanostructure parameters, while GMs can become quasi-GMs through Brillouin zone folding by varying the period of the unit cell, thereby opening the diffraction channel. Since the Q values of quasi-GMs typically follow an inverse square scaling law against the asymmetry parameter, similar to that of symmetry-protected BICs, many studies do not differentiate

between them and refer to both collectively as quasi-BICs [16, 17, 22, 23]. It should be noted that, with the continuous advancement of research, BICs and GMs have gradually been distinguished as separate concepts [21]. However, in practical samples, due to the large functional areas of the periodic nanoarrays, the Q values determined by the aforementioned inverse square law are highly susceptible to sample fabrication defects, resulting in a reduction of the actual Q values.

To enhance the attainable Q factors of quasi-BICs or quasi-GMs in periodic nanostructures, various design strategies have been proposed [24–39]. One approach is to reduce fabrication errors by etching low-index photoresist layers instead of high-index dielectric materials, but the durability of photoresist materials is poor, and BICs cannot be realized [27, 28]. Another approach is to enhance the robustness of the Q factor of the resonance against perturbations, such as by constructing merged BICs through topological charge merging [30–33]. Despite that, merging multiple BICs is commonly observed in periodic arrays with different symmetries; not all eigenmodes of interest can be used to construct merged BICs. Additionally, designing topological charge merging requires precise control over the resonator's structural parameters. By combining two approaches, Watanabe et al. employed shallow-etched structures to suppress radiation losses induced by fabrication disorder in high-order quasi-BIC modes, thereby enhancing the Q factor by an order of magnitude compared to conventional designs [29]. Similarly, Zhou et al. achieved ultrahigh-Q quasi-BICs in dielectric metasurfaces by precisely controlling structural asymmetry through angular perturbation [40]. These advancements have further stimulated efforts to develop new strategies for enhancing the Q factors of experimentally realizable symmetry-protected quasi-BICs and quasi-GMs. Recently, BICs and quasi-GMs induced by Brillouin zone folding have enabled enhanced Q factors across the entire momentum space through employing smaller asymmetric perturbation parameters (α) [21, 34–37], although precisely controlling such small asymmetry parameters during practical sample fabrication remains challenging. Therefore, further investigation is required to develop efficient strategies for enhancing the Q factors of quasi-BICs and quasi-GMs simultaneously under significant symmetry-breaking conditions.

Here, we theoretically propose and experimentally demonstrate an approach to enhance the Q factors of BICs and quasi-GMs via rationally engineered symmetry-breaking in amorphous silicon (α-Si) metasurfaces. For the same wavevector k and asymmetry factor α, theoretical calculations indicate that the Q factors of quasi-BICs and quasi-GMs in metasurfaces realized according to our strategy are enhanced by more than an order of magnitude compared to those achieved via the conventional Brillouin zone folding approaches. Group symmetry analysis of the eigenmodes reveals the formation mechanisms of BICs and quasi-GMs. By employing rational symmetry breaking to preserve the *pmg* space group symmetry of the perturbed metasurface and to enable selective excitation of eigenstates according to symmetry rules, the coupling strength between the resonant state and the far field is suppressed, thereby enhancing the Q factor. The effectiveness of our strategy is experimentally verified by achieving a quasi-GM with a Q factor of $\approx$ 1394 at an asymmetry parameter of 0.2, representing a substantial enhancement over a conventional Brillouin zone folding-induced quasi-GM ($Q \approx 200$) under comparable conditions. Our findings offer a straightforward approach to realizing high-Q resonances and can be extended to enhance light-matter interactions in a variety of optical applications with diverse design requirements.

2 | Results and Discussions

A conventional method for constructing Brillouin zone folding-induced guided resonances involves adjusting the spacing between neighboring nanobricks to double the period of the original unperturbed metasurface in the x-direction, causing the guided modes at the X point to collapse to the Γ point (Figure 1a, middle panel, type-II) [34]. Here, we consider a metasurface consisting of high-index α-Si nanoscatterers embedded in a homogeneous air medium. As shown in Figure 1a, for the unperturbed metasurface of type I, the period dimensions are $p_x/2 = 400$ nm and $p_y = 420$ nm. The square nanobricks have dimensions of $l = 240$ nm and a thickness of $t = 570$ nm, and a gap of $g = p_x/2 - l = 160$ nm. The unperturbed metasurface supports guided modes under the light line, as illustrated in the color scatter plot with thicker edges in Figure 1b. The period of the conventional Δg-perturbed metasurface (Type-II) is $p_x = 800$ nm, and the spacing between the nanobricks in a unit cell is $g-\Delta g$. The asymmetry factor of the Δg-perturbed metasurface is defined as $\alpha_g = \Delta g/g$ [34]. Instead, we construct Brillouin zone folding by deliberately perturbing the structure to form trapezoidal nanobricks, while preserving the 180° rotational symmetry of C_2 (Figure 1a, bottom panel, type-III). The asymmetry factor of the Δl-perturbed metasurface (Type-III) is defined as $\alpha_L = 2\Delta l/l$ [41]. Although both symmetry-breaking methods can convert guided modes below the light line into BICs or quasi-GMs (TM_1, TM_2, TE_1, TE_2) above the light line through band folding, the robustness of the Q values of the generated resonant states with respect to the wavevector k and the asymmetry factor α is different. As shown in Figure 1c, when the asymmetry factor $\alpha = 0.05$, the Q factors of the quasi-BIC mode TM_2 in the proposed Δl-perturbed metasurface as a function of the wavevector k_x are more than an order of magnitude higher than those of the TM_2 mode in the Δg-perturbed metasurface and the unfolded modes in both metasurfaces. The same Q factor enhancement for the quasi-GMs is observed, as shown in Figure 1d. Specifically, for both perturbation methods, the Q factor of the quasi-GM TE_1 mode is inversely proportional to the square of the asymmetry factor α. The fitted coefficient A_2 is approximately ten times larger than A_1, indicating an improvement of more than one order of magnitude over the traditional method across different asymmetry factors. It is important to note that band folding can also be achieved by perturbing the size of the diatomic metasurface traditionally. However, its Q factors demonstrate less robustness compared with those of the Δg-perturbed metasurface; therefore, it will not be discussed further (Figure S1) [34].

Achieving resonance with a higher Q factor requires considering the effects of all structural parameters and wavevector variations on the resonance. We begin by investigating the radiation characteristics of the TM_1, TM_2, and TE_1 modes as functions of the momentum k and the asymmetry factor α, as shown in Figure 2. Figure 2a,c shows that the Q values of the TM_1 and TE_1 modes

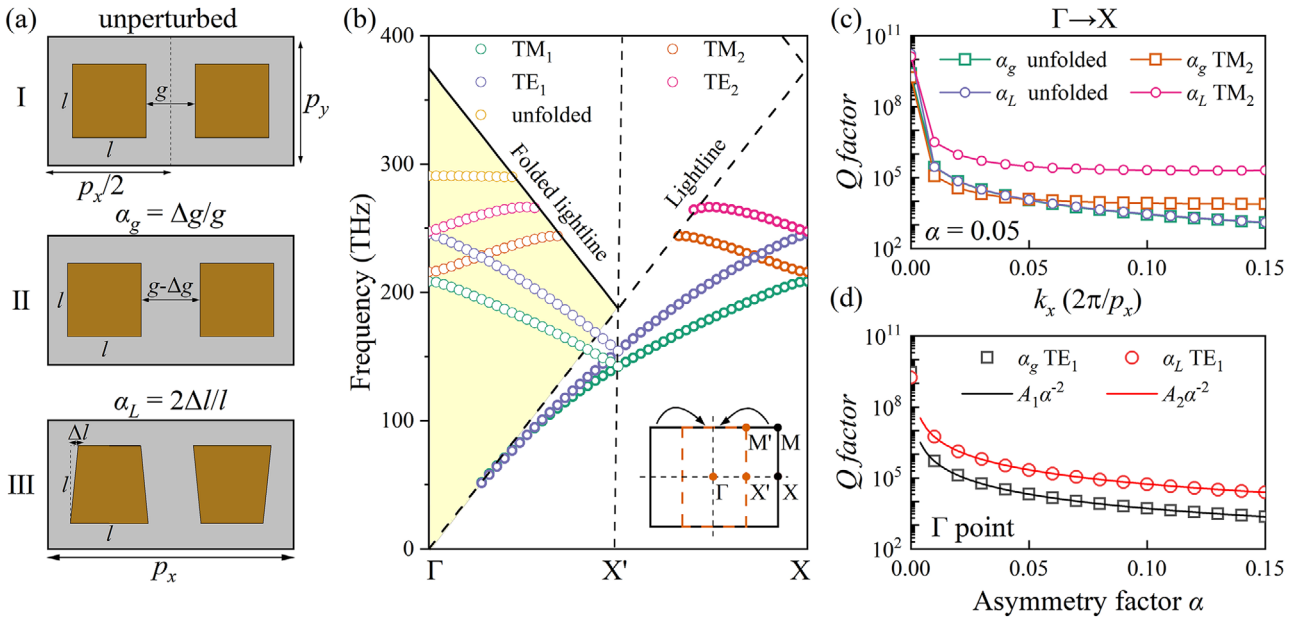

FIGURE 1 | Perturbation methods for the design of symmetry-breaking dielectric metasurfaces with high-Q quasi-BICs and quasi-GMs via Brillouin zone folding. (a) Schematic of the designed unperturbed (type I, top), conventional Δg-perturbed (type II, middle), and the proposed Δl-perturbed (type III, bottom) metasurfaces. (b) Band structure of the unperturbed (perturbed) metasurfaces in the ΓX (X') directions. The color scatter plots with thick and thin edges represent the band structure of the unperturbed and perturbed metasurfaces, respectively. The yellow area represents the zero-order radiation domain of the perturbed metasurfaces. The inset at the bottom right shows the original and folded first Brillouin zone. (c) Calculated Q factor distribution for the unfolded and folded modes (TM$_2$, $\alpha = 0.05$) of two kinds of symmetry-breaking metasurfaces with the variation of wavevector k_x. (d) Calculated Q factor distribution (TE$_1$, Γ point) of two kinds of symmetry-breaking metasurfaces with the variation of asymmetry factor α. The solid lines are fitting curves with $Q \propto \alpha^{-2}$. Here, TE (transverse electric) and TM (transverse magnetic) modes are defined by the presence of only out-of-plane magnetic field (H_z) and electric field (E_z) components, respectively.

decrease gradually with increasing α_g and exhibit minimal variation with momentum k_x, indicating that these modes correspond to quasi-GMs formed by Brillouin zone folding [21, 34, 36]. In contrast, the Q values of the TM$_2$ mode near the Γ point approach infinity for different α_g, corresponding to the symmetry-protected BIC induced by band folding. As shown in Figure 2b, when α_g is nonzero, the Q values of TM$_2$-BIC gradually decrease with increasing wavevector k_x, exhibiting typical quasi-BIC evolution characteristics. Similarly, the three corresponding modes in our proposed Δl-perturbed metasurface align with the same quasi-GM and BIC modes, but exhibit higher Q values, as shown in Figure 2g–i. For the same modes and fixed asymmetry factors, the Q factors of our proposed design are enhanced by more than one order of magnitude compared to the conventional Δg-perturbed metasurface across the entire k-space, so it is more promising to achieve high-Q resonance at large asymmetry factors. The calculation of the radiation characteristics for other eigenmodes in the metasurface is provided in Figure S2, demonstrating that our design enhances the Q factors for various guided resonances in the system.

To further illustrate the distinction between the quasi-GMs and BICs induced by the band folding, we analyze the far-field polarization state distributions of the three eigenmodes in the Δl-perturbed metasurface at $\alpha_L = 0.05$. A BIC corresponds to a far-field polarization singularity that carries a quantized topological charge, which can be defined as $q = \frac{1}{2\pi}\oint_C dk \cdot \nabla_k \phi(k)$, where C is a closed loop in momentum space surrounding the singularity in a counterclockwise direction. Here, $\phi(k) = \frac{1}{2}\arg[S_1(k) + iS_2(k)]$ represents the angle of polarization vector at wavevector $\boldsymbol{k}$ and S_i denotes the Stokes parameters of the far-field polarization vector [15, 42]. As shown in Figure 2d–f, the far-field polarization distributions of the TM$_1$ and TE$_1$ modes exhibit uniform and mutually orthogonal linear polarization states, with no polarization singularities, indicating that they are quasi-GM resonances. In contrast, the far-field distribution of the TM$_2$ mode reveals the presence of a polarization singularity with a topological charge of −1 at the Γ point, corresponding to the BIC state induced by band folding.

To further elucidate the mechanism underlying the transition from GMs to quasi-GMs or BICs induced by the band folding, we conduct a group symmetry analysis on the unperturbed metasurface and two distinct perturbed metasurfaces [17, 43, 44]. The field profiles of the unperturbed metasurface at the X point and the perturbed metasurfaces at the Γ point are shown in Figure 3. Here, we characterize the in-plane symmetries of the TE and TM modes using the out-of-plane magnetic field H_z and the out-of-plane electric field E_z, respectively [17]. (The specific group symmetry analysis is provided in Figure S3). For the original unperturbed metasurface, there are two types of C_2 rotation centers: C_2^m, located at the midpoint between two neighboring nanobricks, and C_2^c, located at the center of a single nanobrick. As an example, the TM$_1$ mode in the unperturbed metasurface exhibits a B_2 irreducible representation with respect to the rotation center C_2^m and the mirror surfaces passing through

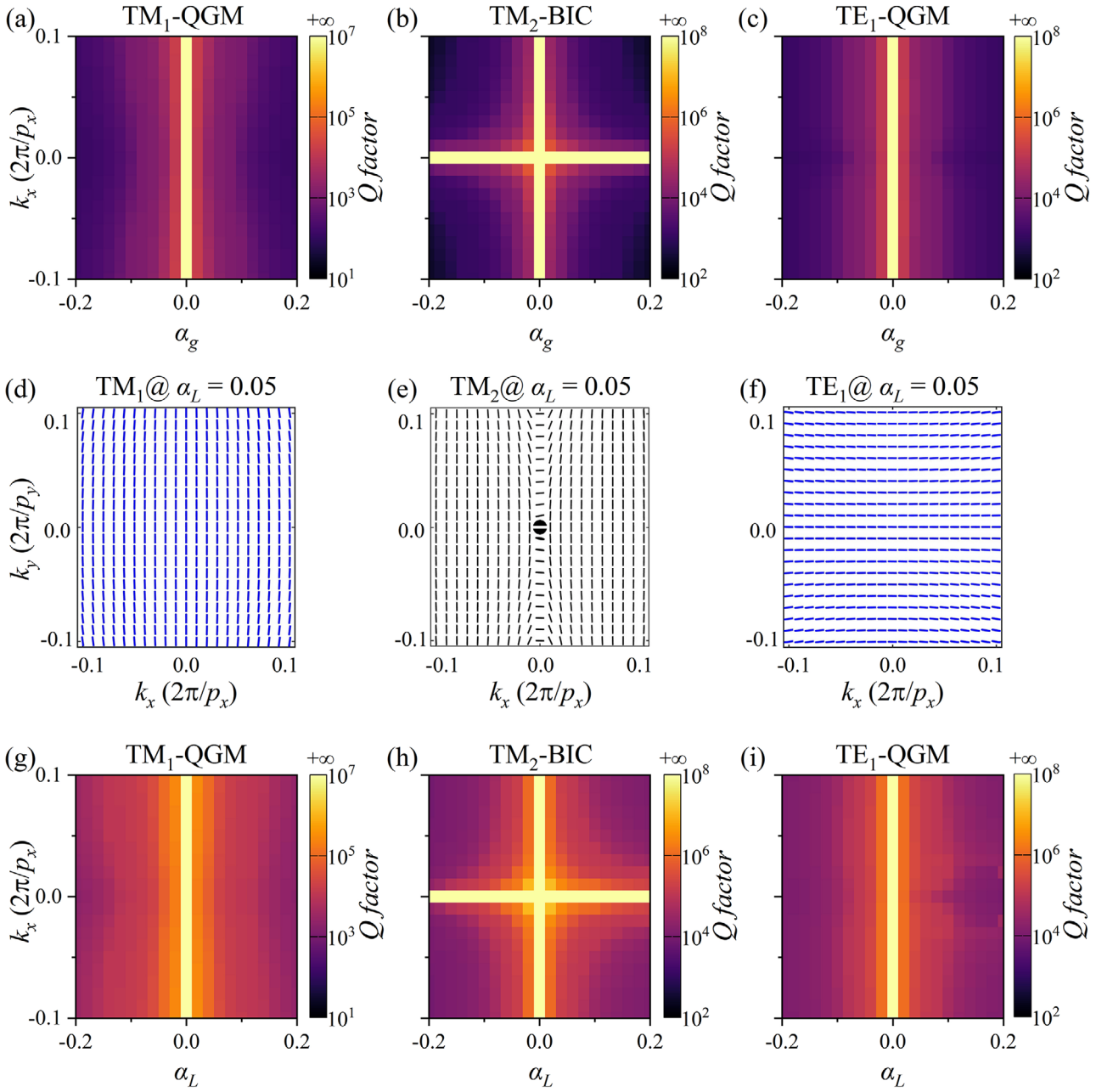

FIGURE 2 | Enhancement of the Q factors for quasi-GMs and BICs through symmetry-breaking metasurfaces. (a–c) Calculated Q factor distributions of TM_1-QGM, TM_2-BIC, and TE_1-QGM modes supported by traditional Δg-perturbed metasurface as functions of wavevector k_x and asymmetry factor α_g. The QGM represents the quasi-GM resonance. (d–f) Calculated far-field polarization state distributions of three corresponding eigenmodes in momentum space supported by Δl-perturbed metasurface for $\alpha_L = 0.05$. (g–i) Calculated Q factor distributions of three corresponding eigenmodes supported by the proposed Δl-perturbed metasurface as functions of wavevector k_x and asymmetry factor α_L.

it, and an A_1 irreducible representation with respect to the C_2^c. For metasurfaces perturbed by either Δl or Δg, the rotation center C_2^m is preserved, while C_2^c symmetry is broken, thereby maintaining the same selection rule [34, 37]. Since the TM_1 modes in the perturbed metasurfaces exhibit odd parity about the unique center of rotation C_2^m, they can couple to the normal excitation plane wave with odd parity, behaving as quasi-GMs with finite Q values. This condition is similarly satisfied for the TE_1 modes. However, for the TM_2 modes in the perturbed metasurfaces, their A_1 irreducible representations correspond to even parity and thus cannot couple to the normally incident plane wave, leading to the formation of symmetry-protected BICs at the Γ point. Therefore, the group symmetry analysis clearly explains why the same modes in the two perturbed metasurfaces behave as identical quasi-GMs or BICs, rather than as the opposite. This clarification facilitates the comparison of Q values for eigenmodes with different band folding methods [17, 34].

Although the two perturbed metasurfaces share the same center of rotation as the unperturbed metasurfaces, their other symmetry elements differ, resulting in distinct space groups [43]. Due to the presence of the glide reflection operation, the proposed

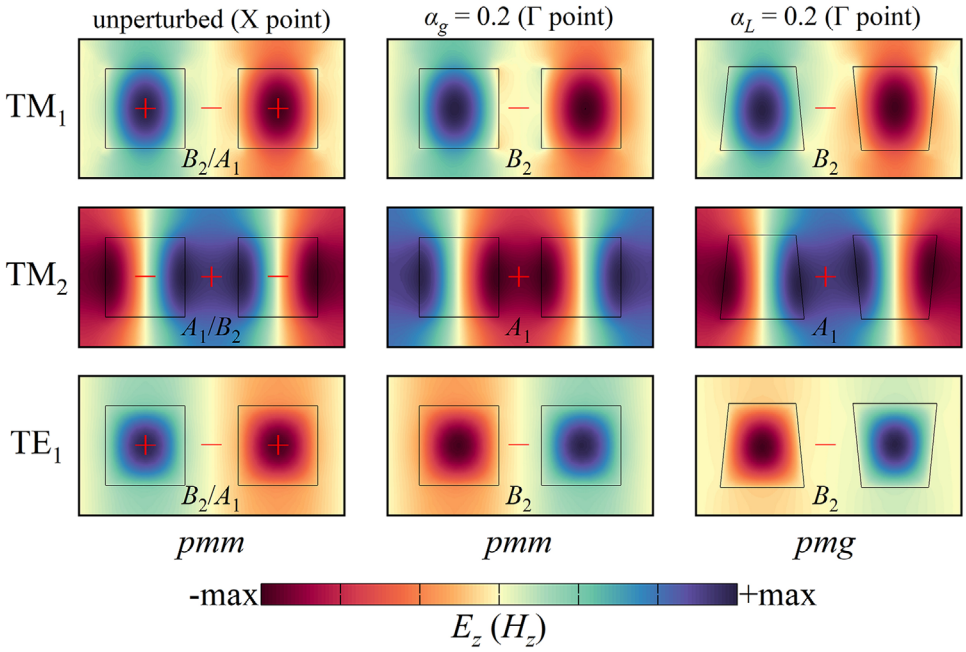

FIGURE 3 | Group symmetry analysis of eigenmodes supported by the unperturbed and perturbed metasurfaces. Calculated electric field profiles E_z (TM$_1$ and TM$_2$ modes) and magnetic field profiles H_z (TE$_1$ mode) at the X point for the unperturbed metasurface (left panel) and Γ point for the Δ*g*-perturbed ($\alpha_g = 0.2$, middle panel) and Δ*l*-perturbed ($\alpha_L = 0.2$, right panel) metasurfaces. The A_n/B_n ($n = 1,2$) represent the irreducible representations of three eigenmodes according to the point group theory. And the signs '+' and '−' represent the mode profiles that own even and odd symmetry under the C_2 operation.

Δ*l*-perturbed metasurface corresponds to the space group *pmg*, which differs from the *pmm* space group of the Δ*g*-perturbed metasurface. This difference contributes to the increased *Q* factor robustness of the Δ*l*-perturbed metasurface. This robustness can also be observed when the perturbed metasurface maintains the same *pmg* space group symmetry and selection rule. Since controlling the positions of nanostructures during sample fabrication is easier than modifying their geometric shapes [43, 45–47], the same *Q* factor enhancement can be achieved by simply altering the lateral displacement of the nanobricks along the *y*-direction within the perturbed diatomic metasurface unit cell (see Figure S7).

To explain the enhanced *Q* values of the perturbed metasurfaces, we further calculate the overlap between the incident light field and the eigenstate field to characterize the coupling strength between the eigenstate and free space [16]. Taking the TE$_1$ mode as an example, for the proposed Δ*l*-perturbed metasurface, the *Q* values are a magnitude greater than those of the Δ*g*-perturbed metasurface, as shown in Figure 4a. The TE$_1$ mode in two perturbed metasurfaces can be excited by *x*- and *y*-polarized plane waves, respectively, and the field distributions at the resonant wavelength exhibit a significant enhancement of the electric field, as shown in Figure 4b,c. This strong near-field enhancement can be utilized to improve harmonic generation efficiency, as illustrated in the Section S4. To quantify the far-field coupling strength, we employ the multipole expansion method for the eigenstates, calculating the electric dipole moments $\boldsymbol{p}$, magnetic dipole moments $\boldsymbol{m}$, and electric quadrupole moments $\boldsymbol{Q}$ within the unit cell (Detailed expressions are presented in Section S5). For plane waves with *x*- and *y*-polarizations and wavevector along the *z*-direction, the corresponding far-field coupling amplitudes c_x and c_y can be expressed as [16]:

$$c_x \propto -\frac{k_0}{\sqrt{2S_0}}\left(p_x - \frac{m_y}{c} + \frac{ik_0}{6}Q_{zx}\right)$$
$$c_y \propto -\frac{k_0}{\sqrt{2S_0}}\left(p_y + \frac{m_x}{c} + \frac{ik_0}{6}Q_{yz}\right)$$

The radiation losses can be expressed as:

$$\gamma_{rad} \propto c\left(|c_x|^2 + |c_y|^2\right)$$

where $k_0 = \omega_0/c$ is the free space wavevector with ω_0 is the resonant frequency and *c* is the velocity of light in free space. S_0 is the unit cell area. $c_{x,y}$ are the coupling amplitudes between eigenstates and the zero-order diffraction channels of *x*- and *y*-polarized incident light. Figure 4d,e shows the contributions of different multipolar components to the far-field coupling. It can be observed that the TE$_1$ modes in the metasurfaces perturbed by Δ*l* and Δ*g* are primarily coupled with the dipole moments along the *x*- and *y*-directions, respectively, which is consistent with the spectral excitation dependence results shown in Figure 4b. Moreover, we observe that the magnitude of p_y are three times greater than that of p_x under the same asymmetry factor. Consequently, Figure 4f shows that the radiation factor of the Δ*g*-perturbed metasurface is a magnitude higher than that of the Δ*l*-perturbed metasurface. These results correspond to a magnitude increase in the *Q* factors shown in Figure 4a, which is attributed to the dependence of the *Q* values on the

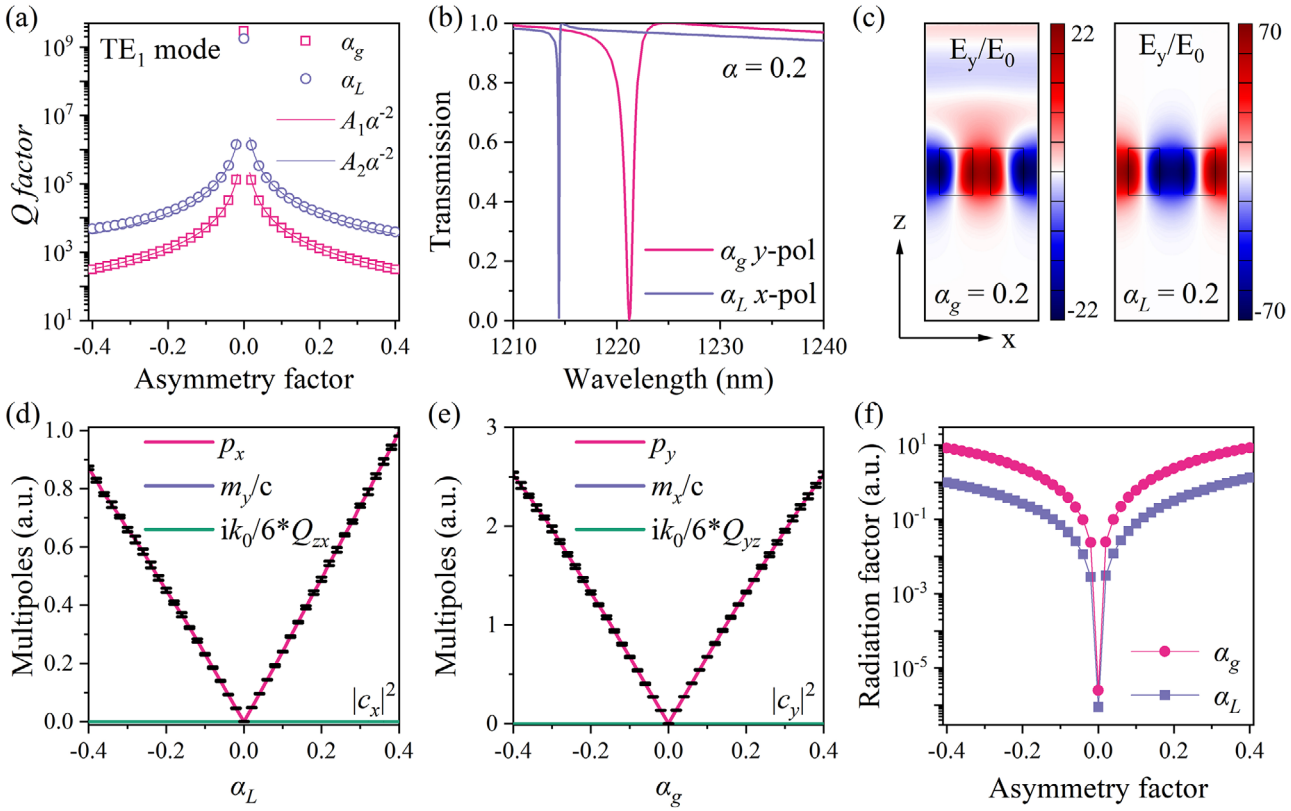

FIGURE 4 | Far-field couple amplitude calculation of eigenstate. (a) Calculated Q factor distribution of the TE_1 mode as functions of asymmetry factor α and (b) the corresponding transmission spectra at $\alpha = 0.2$. The solid lines in (a) represent fitting curves, where $Q \propto \alpha^{-2}$. (c) Calculated modal electric field profile E_y of the TE_1 mode supported by the Δg-perturbed ($\alpha_g = 0.2$, left panel) and Δl-perturbed ($\alpha_L = 0.2$, right panel) metasurfaces. (d,e) Calculated the normalized multipole components of the coupling amplitudes c_x and c_y for the Δg-perturbed and Δl-perturbed metasurfaces as a function of the asymmetry factor. The black error bars represent the numerical uncertainties arising from variations in the integration volume. (f) Calculated radiation factor γ_{rad} as functions of the asymmetry factor α_g and α_L at the Γ point.

square of the asymmetry factor α. Therefore, our proposed Δl-perturbed metasurface can effectively enhance the Q factors of guided resonances by suppressing radiation losses.

To demonstrate the effectiveness of our proposed design in enhancing the resonant Q values, we further fabricated α-Si metasurfaces on silica substrate with varying asymmetric parameters for experimental measurements, as shown in the side-view scanning electron microscope (SEM) images in Figure 5a. Metasurfaces perturbed by Δl and Δg, with 100 × 100 periods, were fabricated with asymmetry factors α = 0.5, 0.35, and 0.2. A custom-built optical setup was used to measure the free-space transmission spectrum of the samples (More details can be found in the Experimental Section and Figure S5).

Here, we focus on the TM_1-QGM mode with a resonant wavelength of approximately 1550 nm in both types of symmetry-breaking metasurfaces. Figure 5b illustrates the simulated and measured transmission spectra of the metasurface perturbed by Δg for different asymmetry factors. As the asymmetry factor α_g increases, the resonance linewidth gradually broadens, resulting in a decrease in the Q factors. We employed the Fano formula to fit the transmission spectrum and determine the Q values corresponding to asymmetry factors (α_g) of 0.5, 0.35, and 0.2, which yielded Q values of 17, 56, and 200, respectively (see Figure S6) [16, 26, 37]. It is noteworthy that as α_g increases, the measured resonance wavelength exhibits a progressively larger redshift compared to the theoretical results. This discrepancy may arise from the larger dimensions of the nanobricks due to sample fabrication errors. Furthermore, this effect becomes more pronounced when the distance between adjacent nanobricks is reduced. For the metasurface perturbed by Δl, the experimentally obtained Q values corresponding to asymmetry factors (α_L) of 0.5, 0.35, and 0.2 are 637, 676, and 1,394, respectively, as shown in Figure 5c. These values are significantly higher than those of the metasurface perturbed by Δg under the same asymmetry conditions. It should be noted that the Q factors obtained in our experiment are limited. In addition to the extra radiation channels introduced by structural disorder and the limited array size during sample fabrication, the direct transmission spectroscopy method is also restricted by its spectral resolution [26, 35]. Therefore, fabricating samples with smaller asymmetry factors, adjusting the y-direction spacing of the nanostructures to tune symmetry (see Figure S7), and employing cross-polarization scattering measurements may experimentally yield higher Q factors [30, 39]. To more clearly demonstrate the enhancement in the Q factor achieved by our proposed rationally symmetry-breaking metasurface, the Q values under various asymmetry factors were extracted from the transmission spectra in Figure 5b,c, as summarized in Figure 5d. The Q values for α_L = 0.2 are approximately seven times greater than those for $\alpha_g = 0.2$. These results highlight the significant advantage of our proposed Δl-

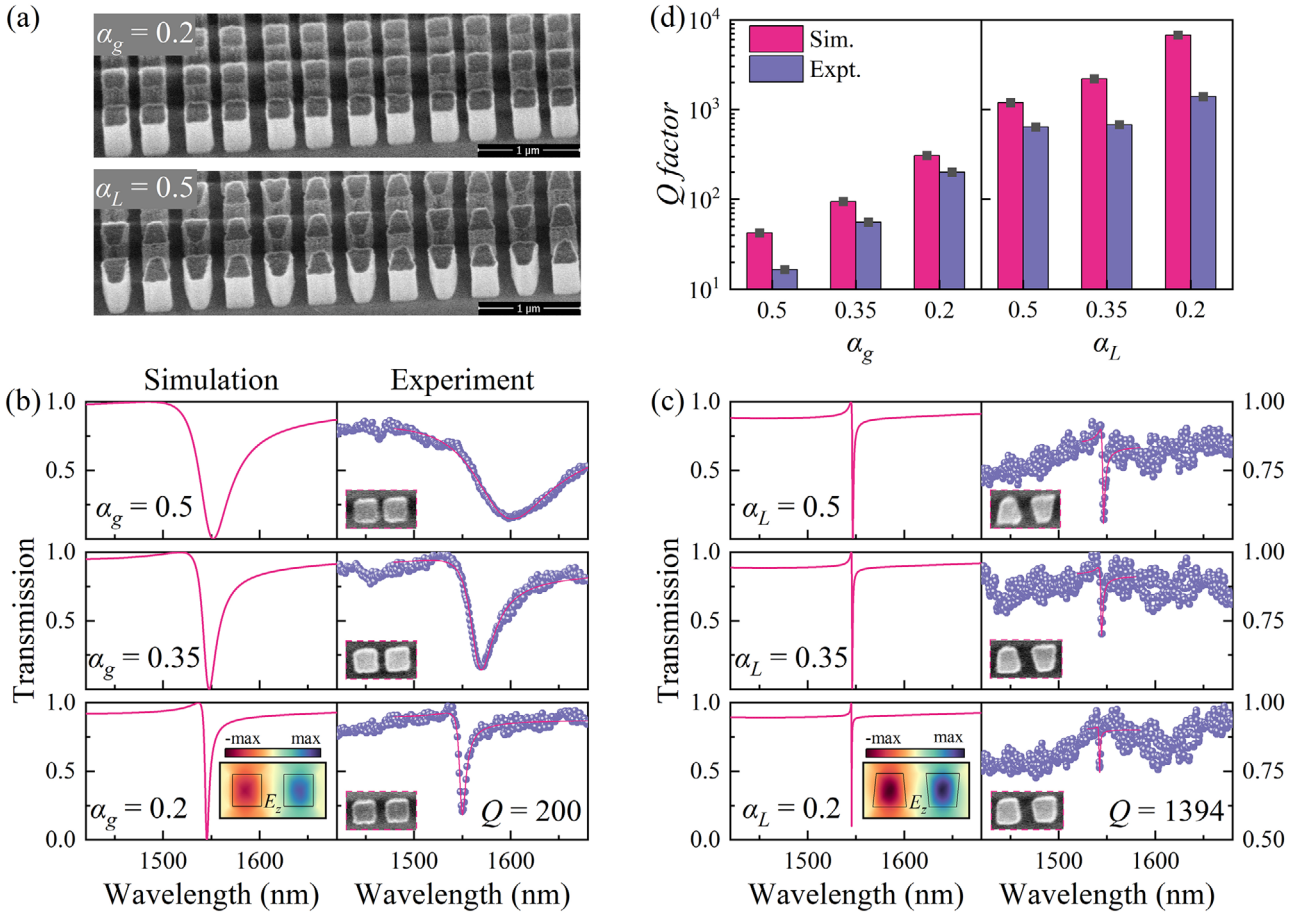

FIGURE 5 | Experimental demonstration of the enhanced high-Q factor quasi-GMs. (a) SEM images of the fabricated Δg-perturbed ($\alpha_g = 0.2$, top panel) and Δl-perturbed ($\alpha_L = 0.5$, bottom panel) metasurfaces. (b,c) Numerically simulated (left panel) and experimentally measured (right panel) transmission spectra for two kinds of symmetry-breaking metasurfaces with asymmetry factor $\alpha = 0.5$, 0.35, and 0.2. The magenta line in the measured transmission spectra represents the Fano fitting results. The insets in the left panel show the distribution of the out-of-plane electric field components in the x-y plane for the simulated TM_1 modes at $\alpha = 0.2$. The bottom-left insets in the right panel present SEM images of unit cells with different asymmetry factors. (d) Simulated and experimentally extracted Q factors from the transmission spectra as a function of the asymmetry factor.

perturbed metasurface in enhancing Q values under identical asymmetry factors.

3 | Conclusions

To conclude, we have both theoretically and experimentally demonstrated an efficient design strategy to simultaneously improve the Q factors of quasi-BICs and quasi-GMs induced by Brillouin zone folding. Theoretical calculations indicate that the Q factors of these modes perturbed according to our strategy are enhanced by more than an order of magnitude compared to those perturbed via the conventional Brillouin zone folding approach under the same wavevector k and asymmetry factor α. Experimentally, we achieved a quasi-GM with a Q factor of 1394 when the asymmetry factor is 0.2, representing a substantial increase compared to the Q factor of 200 obtained with the conventional design. Our strategy is based on rational breaking of certain symmetries of the original lattice while preserving others. It is highly efficient and applicable to all BICs and quasi-GMs. This method can be further extended to various spectral bands and configurations, providing a promising avenue for enhancing the performance of nanophotonic devices.

4 | Experimental Section

4.1 | Sample Fabrication

The dielectric α-Si symmetry-breaking metasurfaces were fabricated on a meticulously prepared fused quartz substrate. First, a 570-nm-thick hydrogenated amorphous silicon (a-Si: H) film was deposited onto the substrate using plasma-enhanced chemical vapor deposition (Plasmalab 100 from Oxford). Following spin-coating with an electron beam resist (ZEP520A, Zeon Chemicals), a thin layer of e-spacer 300Z (Showa Denko) was applied to mitigate charging effects during subsequent electron beam exposure. Subsequently, the metasurface patterns were created through electron-beam lithography (ELS-BODEN 125 from STS-Elionix) and development. Next, a 70 nm-thick aluminum (Al) layer was deposited by electron beam evaporation (Temescal BJD-2000), followed by extraction of the sample through immersion in resist (ZDMAC from ZEON Co.). Finally, the remaining Al

pattern array was used as an etching mask, and the designed pattern was transferred to the a-Si: H film using plasma reactive ion etching (a mixture of CHF_3 and SF_6). The residual Al etching mask was then removed with an aluminum wet etching solution (a mixture of H_3PO_4, HNO_3, acetic acid, and water).

4.2 | Numerical Simulations

All numerical simulations were performed using the commercial software COMSOL Multiphysics based on the finite element method. The band structures and Q factors were obtained using the eigenfrequency solver, with the Q factor extracted from the complex eigenfrequency ω according to $Q = \mathrm{Re}(\omega)/2[\mathrm{Im}(\omega)]$. In the computational 3D full-vector model, both polarizations were investigated: modes were classified according to their dominant out-of-plane field components (TE-like and TM-like). For the band structure calculation, the k-point sampling resolution $\Delta k = 0.01 \cdot (2\pi/\text{period})$. Periodic (Floquet) boundary conditions were applied along the x and y directions of the unit cell, while perfectly matched layers were imposed along the z direction. To ensure convergence (relative tolerance $= 1 \times 10^{-6}$) in the calculation of eigenmodes with extremely high Q factors, a physics-controlled mesh with a normal element size was employed, and the maximum mesh element size was constrained by setting a maximum frequency of 600 THz. The refractive indices of α-Si and the SiO_2 substrate were set as 3.48 and 1.45, respectively [30]. Therefore, the absorptive losses of the materials in the simulation were ignored, and the total Q factor is equal to the radiative Q factor.

4.3 | Optical Characterizations

The free-space transmission spectra of the symmetry-breaking metasurfaces were measured using a custom-built optical setup, as shown in Figure S4. A supercontinuum laser (NKT SuperK, EXR-20) was incident on the fabricated sample through a fiber collimator and an infrared broadband linear polarizer (Codixx AG, IR 1300 BC5) to generate linearly polarized light. The output beam was collected through an objective lens (Sigma NIR Program Apo 20×, NA = 0.45), passed through an aperture and another lens, and then directed to a spectrum analyzer (Zolix, Omni750i) via a fiber coupler. The aperture is used to control the measurement area, which is slightly smaller than the sample size. A switchable mirror was placed behind the lens to alternate between sample imaging, captured by a CMOS camera (TUCSEN, Mlchrome 5BW), and spectral measurements. Transmission intensity data were obtained using the optical spectrum analyzer software. The collected data were normalized by dividing the air background spectrum to obtain the final transmission spectrum.

Acknowledgements

This work was supported by the National Key Research and Development Program of China (2024YFA1409903 and 2021YFA1400601), the National Natural Science Foundation of China (12192253, 12274237, 12274239, 12474331, and U22A20258), and the Natural Science Foundation of Tianjin (22JCZDJC00400, 22JCYBJC00800, and 22JCYBJC01350).

Conflicts of Interest

The authors declare no conflict of interest.

Data Availability Statement

The data that support the findings of this study are available from the corresponding author upon reasonable request.

References

1. J. Yu, W. Yao, M. Qiu, and Q. Li, "Free-space High-Q Nanophotonics," *Light: Science & Applications* 14 (2025): 174, https://doi.org/10.1038/s41377-025-01825-x.

2. S. Wu, S. Buckley, J. R. Schaibley, et al., "Monolayer Semiconductor Nanocavity Lasers with Ultralow Thresholds," *Nature* 520 (2015): 69–72.

3. M. Wu, L. Ding, R. P. Sabatini, et al., "Bound State in the Continuum in Nanoantenna-Coupled Slab Waveguide Enables Low-Threshold Quantum-Dot Lasing," *Nano Letters* 21 (2021): 9754–9760, https://doi.org/10.1021/acs.nanolett.1c03696.

4. M. S. Hwang, H. C. Lee, K. H. Kim, et al., "Ultralow-Threshold Laser Using Super-Bound States in the Continuum," *Nature Communications* 12 (2021): 4135.

5. Y.-C. Lee, Y.-L. Ho, B.-W. Lin, et al., "High-Q Lasing via All-Dielectric Bloch-Surface-Wave Platform," *Nature Communications* 14 (2023): 6458, https://doi.org/10.1038/s41467-023-41471-8.

6. Z. Liu, Y. Xu, Y. Lin, et al., "High-Q Quasibound States in the Continuum for Nonlinear Metasurfaces," *Physical Review Letters* 123 (2019): 253901, https://doi.org/10.1103/PhysRevLett.123.253901.

7. I. Toftul, P. Tonkaev, K. Koshelev, et al., "Chiral Dichroism in Resonant Metasurfaces with Monoclinic Lattices," *Physical Review Letters* 133 (2024): 216901, https://doi.org/10.1103/PhysRevLett.133.216901.

8. Y. Zang, R. Chai, W. Liu, et al., "Enhanced Wide-angle Third-harmonic Generation in Flat-band-engineered Quasi-BIC Metagratings," *Science China Physics, Mechanics & Astronomy* 67 (2024): 244212, https://doi.org/10.1007/s11433-023-2299-9.

9. X. Sun, J. Sun, Z. Wang, L. Wang, F. Qiu, and L. Wen, "Manipulating Dual Bound States in the Continuum for Efficient Spatial Light Modulator," *Nano Letters* 22 (2022): 9982–9989, https://doi.org/10.1021/acs.nanolett.2c03539.

10. I. C. Benea-Chelmus, S. Mason, M. L. Meretska, et al., "Gigahertz Free-Space Electro-Optic Modulators Based on Mie Resonances," *Nature Communications* 13 (2022): 3170, https://doi.org/10.1038/s41467-022-30451-z.

11. V. Ardizzone, F. Riminucci, S. Zanotti, et al., "Polariton Bose–Einstein Condensate from a Bound State in the Continuum," *Nature* 605 (2022): 447–452.

12. T. Weber, L. Kühner, L. Sortino, et al., "Intrinsic Strong Light-matter Coupling with Self-Hybridized Bound States in the Continuum in van der Waals Metasurfaces," *Nature Materials* 22 (2023): 970–976, https://doi.org/10.1038/s41563-023-01580-7.

13. A. M. Berghuis, G. W. Castellanos, S. Murai, et al., "Room Temperature Exciton–Polariton Condensation in Silicon Metasurfaces Emerging From Bound States in the Continuum," *Nano Letters* 23 (2023): 5603–5609, https://doi.org/10.1021/acs.nanolett.3c01102.

14. C. W. Hsu, B. Zhen, A. D. Stone, J. D. Joannopoulos, and M. Soljačić, "Bound States in the Continuum," *Nature Reviews Materials* 1 (2016): 16048, https://doi.org/10.1038/natrevmats.2016.48.

15. J. Wang, P. Li, X. Zhao, et al., "Optical Bound States in the Continuum in Periodic Structures: Mechanisms, Effects, and Applications," *Photonics Insights* 3 (2024): R01.

16. K. Koshelev, S. Lepeshov, M. Liu, A. Bogdanov, and Y. Kivshar, "Asymmetric Metasurfaces With High-Q Resonances Governed by Bound

States in the Continuum," *Physical Review Letters* 121 (2018): 193903, https://doi.org/10.1103/PhysRevLett.121.193903.

17. A. C. Overvig, S. C. Malek, M. J. Carter, S. Shrestha, and N. Yu, "Selection Rules for Quasibound States in the Continuum," *Physical Review B* 102 (2020): 035434, https://doi.org/10.1103/PhysRevB.102.035434.

18. Y. Liang, D. P. Tsai, and Y. Kivshar, "From Local to Nonlocal High-Q Plasmonic Metasurfaces," *Physical Review Letters* 133 (2024): 053801, https://doi.org/10.1103/PhysRevLett.133.053801.

19. R. Chai, Q. Liu, W. Liu, et al., "Emerging Planar Nanostructures Involving both Local and Nonlocal Modes," *ACS Photonics* 10 (2023): 2031–2044, https://doi.org/10.1021/acsphotonics.2c01534.

20. L. Huang, L. Xu, D. A. Powell, W. J. Padilla, and A. E. Miroshnichenko, "Resonant Leaky Modes in All-Dielectric Metasystems: Fundamentals and Applications," *Physics Reports* 1008 (2023): 1–66, https://doi.org/10.1016/j.physrep.2023.01.001.

21. K. Sun, H. Wei, W. Chen, et al., "Infinite-Q Guided Modes Radiate in the Continuum," *Physical Review B* 107 (2023): 115415, https://doi.org/10.1103/PhysRevB.107.115415.

22. D. R. Abujetas, N. van Hoof, S. ter Huurne, J. G. Rivas, and J. A. Sánchez-Gil, "Spectral and Temporal Evidence of Robust Photonic Bound States in the Continuum on Terahertz Metasurfaces," *Optica* 6 (2019): 996–1001.

23. G. Xu, A. Overvig, Y. Kasahara, E. Martini, S. Maci, and A. Alu, "Arbitrary Aperture Synthesis with Nonlocal Leaky-Wave Metasurface Antennas," *Nature Communications* 14 (2023): 4380, https://doi.org/10.1038/s41467-023-39818-2.

24. S.-G. Lee, S.-H. Kim, and C.-S. Kee, "Metasurfaces With Bound States in the Continuum Enabled by Eliminating First Fourier Harmonic Component in Lattice Parameters," *Physical Review Letters* 126 (2021): 013601, https://doi.org/10.1103/PhysRevLett.126.013601.

25. R. Chai, W. Liu, Z. Li, et al., "Spatial Information Lasing Enabled by Full-k-Space Bound States in the Continuum," *Physical Review Letters* 132 (2024): 183801, https://doi.org/10.1103/PhysRevLett.132.183801.

26. S. You, H. He, Y. Zhang, et al., "Resonance Wavelength Stabilization of Quasi-Bound States in the Continuum Constructed by Symmetry Breaking and Area Compensation," *Nano Letters* 24 (2024): 15300–15307, https://doi.org/10.1021/acs.nanolett.4c04217.

27. J. Fang, R. Chen, D. Sharp, et al., "Million-Q Free Space Meta-Optical Resonator at Near-Visible Wavelengths," *Nature Communications* 15 (2024): 10341, https://doi.org/10.1038/s41467-024-54775-0.

28. L. Huang, R. Jin, C. Zhou, et al., "Ultrahigh-Q Guided Mode Resonances in an All-dielectric Metasurface," *Nature Communications* 14 (2023): 3433, https://doi.org/10.1038/s41467-023-39227-5.

29. K. Watanabe, T. Nagao, and M. Iwanaga, "Low-Contrast BIC Metasurfaces with Quality Factors Exceeding 100,000," *Nano Letters* 25 (2025): 2777–2784.

30. J. Jin, X. Yin, L. Ni, M. Soljacic, B. Zhen, and C. Peng, "Topologically Enabled Ultrahigh-Q Guided Resonances Robust to Out-of-Plane Scattering," *Nature* 574 (2019): 501–504, https://doi.org/10.1038/s41586-019-1664-7.

31. M. Kang, S. Zhang, M. Xiao, and H. Xu, "Merging Bound States in the Continuum at Off-High Symmetry Points," *Physical Review Letters* 126 (2021): 117402, https://doi.org/10.1103/PhysRevLett.126.117402.

32. L. Huang, B. Jia, Y. K. Chiang, et al., "Topological Supercavity Resonances in the Finite System," *Advanced Science* 9 (2022): 2200257.

33. S. Yu, Z. Li, R. Chai, et al., "Merging Bound States in the Continuum in the Geometrical Parameter Space," *Physical Review B* 109 (2024): 115109, https://doi.org/10.1103/PhysRevB.109.115109.

34. W. Wang, Y. K. Srivastava, T. C. Tan, Z. Wang, and R. Singh, "Brillouin Zone Folding Driven Bound States in the Continuum," *Nature Communications* 14 (2023): 2811, https://doi.org/10.1038/s41467-023-38367-y.

35. S. Li, B. Ma, Q. Li, and M. V. Rybin, "Antenna-Based Approach to Fine Control of Supercavity Mode Quality Factor in Metasurfaces," *Nano Letters* 23 (2023): 6399–6405, https://doi.org/10.1021/acs.nanolett.3c01141.

36. Z. Li, S. Yu, G. Geng, et al., "Chiral Guided Mode Resonance with Independently Controllable Quality Factor and Circular Dichroism," *Nano Letters* 25 (2025): 2519–2527.

37. G. Xu, Z. Xue, J. Fan, et al., "Flexible Terahertz Metasurface Absorbers Empowered by Bound States in the Continuum," *Advanced Materials* 36 (2024): 2470321.

38. S. Yang, M. He, C. Hong, J. D. Caldwell, and J. C. Ndukaife, "Engineering Electromagnetic Field Distribution and Resonance Quality Factor Using Slotted Quasi-BIC Metasurfaces," *Nano Letters* 22 (2022): 8060–8067, https://doi.org/10.1021/acs.nanolett.2c01919.

39. L. Huang, S. Li, C. Zhou, et al., "Realizing Ultrahigh-Q Resonances Through Harnessing Symmetry-Protected Bound States in the Continuum," *Advanced Functional Materials* 34 (2024): 2309982, https://doi.org/10.1002/adfm.202309982.

40. C. Zhou, M. Zhou, Z. Fu, et al., "Ultrahigh-Q Quasi-BICs via Precision-Controlled Asymmetry in Dielectric Metasurfaces," *Nano Letters* 25 (2025): 5916–5924, https://doi.org/10.1021/acs.nanolett.5c00967.

41. W. Liu, B. Wang, Y. Zhang, et al., "Circularly Polarized States Spawning From Bound States in the Continuum," *Physical Review Letters* 123 (2019): 116104, https://doi.org/10.1103/PhysRevLett.123.116104.

42. B. Zhen, C. W. Hsu, L. Lu, A. D. Stone, and M. Soljacic, "Topological Nature of Optical Bound States in the Continuum," *Physical Review Letters* 113 (2014): 257401, https://doi.org/10.1103/PhysRevLett.113.257401.

43. R. Chai, W. Liu, Z. Li, H. Cheng, J. Tian, and S. Chen, "Multiband Quasibound States in the Continuum Engineered by Space-group-invariant Metasurfaces," *Physical Review B* 104 (2021): 075149, https://doi.org/10.1103/PhysRevB.104.075149.

44. K. Sakoda, *Optical Properties of Photonic Crystals* (Springer Science & Business Media, 2004).

45. S. You, M. Zhou, L. Xu, et al., "Quasi-bound States in the Continuum with a Stable Resonance Wavelength in Dimer Dielectric Metasurfaces," *Nanophotonics* 12 (2023): 2051.

46. Y. Zhang, L. Wang, H. He, et al., "High-Q Magnetic Toroidal Dipole Resonance in all-dielectric Metasurfaces," *APL Photonics* 9 (2024): 076106, https://doi.org/10.1063/5.0208936.

47. H. Zhong, L. Huang, S. Li, et al., "Toroidal Dipole Bound States in the Continuum in Asymmetric Dimer Metasurfaces," *Applied Physics Reviews* 11 (2024): 031404.

Supporting Information

Additional supporting information can be found online in the Supporting Information section.

Supporting File: lpor70591-sup-0001-SuppMat.docx.